Compressible magnetohydrodynamic Kelvin–Helmholtz instability with vortex pairing in the two-dimensional transverse configuration

Akira Miura[a)]
Department of Earth and Planetary Physics, University of Tokyo, Bunkyo-ku, Tokyo 113, Japan

(Received 10 February 1997; accepted 6 May 1997)

For a two-dimensional (2-D) transverse configuration, where the plasma motion occurs in a 2-D plane transverse to the magnetic field, the nonlinear evolution of the magnetohydrodynamic (MHD) Kelvin–Helmholtz (K–H) instability is investigated by means of a 2-D MHD simulation for a convective fast magnetosonic Mach number 0.35, which is defined for the total jump of the flow velocity. The compressibility and the nonzero baroclinic vector are shown to violate the conservation of the enstrophy for the 2-D MHD transverse configuration and for the 2-D fluid motion. After the nonlinear saturation of the linearly fastest growing vortices, the vortices continue to coalesce until no more vortex pairing is allowed, owing to a finite length of the simulation system. The plasma inside the vortex is rarefied strongly by the fast magnetosonic rarefaction and each vortex is associated with an eddy current, which is inertia current in nature. The plasma flow velocity is enhanced at the periphery of the vortex and the net momentum transport and shear relaxation by the instability occur as long as the vortex pairing continues. Anomalous viscosity by the K–H instability increases with the vortex pairing and its increase is due to the growth of subharmonic modes. © *1997 American Institute of Physics.* [S1070-664X(97)01708-4]

I. INTRODUCTION

The Kelvin–Helmholtz (K–H) instability[1–5] is driven by the velocity shear in fluids and plasmas and is important in understanding a variety of phenomena involving velocity-sheared flow in space plasmas,[6–39] astrophysical plasmas,[40–50] laboratory plasmas,[51–60] and, of course, fluid dynamics.[61–73] A notable prototype example in space plasmas is the K–H instability excited at the magnetopause between the flowing solar wind plasma and the stationary magnetospheric plasma.[6–15,17,18,20–24,26–36,38,39] The K–H instability at the magnetopause has been suggested to be responsible for driving a plasma circulation inside the magnetoshere and for a tailward stretching of geomagnetic field lines[17,21,24,28,35] on the hypothesis that the nonlinear evolution of the magnetopause K–H instability provides a viscous-like drag[74] or a perpendicular momentum transport at the magnetopause. Although the contribution of the K–H instability to the plasma circulation in the magnetosphere appears to be smaller than that of the reconnection at the magnetopause,[75] it is important to know quantitatively the contribution of the K–H instability to the plasma circulation in the magnetosphere for a complete understanding of the dynamics of the solar wind–magnetosphere interaction. Such an understanding of the contribution of the K–H instability to the magnetospheric plasma circulation may also be important in understanding the plasma dynamics occurring at the boundary between the magnetosphere of the neutron star and the surrounding accretion disk.[40–43,45] Observational evidence supporting the occurrence of the K–H instability at the terrestrial and planetary magnetopauses has been accumulated.[76–84] Complete understanding of the nonlinear evolution of magnetohydrodynamic (MHD) waves excited by the K–H instability at the velocity shear in plasmas is also important in understanding the origin of MHD waves observed in the solar wind.[18,85,86] In fusion plasmas, complete understanding of the $\mathbf{E}\times\mathbf{B}$ shear stabilization and/or destabilization of turbulence at the plasma boundary is also important in improving plasma confinement in tokamak[87] and stellarator plasmas. It is important to note here that in space and astrophysical plasmas the total velocity jump across the velocity shear layer has large sonic and Alfvénic Mach numbers.[88] Therefore, it is essentially necessary in such cases to take into account the compressibility of the plasmas.

The study of the K–H instability has a long history in hydrodynamics. It is well known that in the two-dimensional (2-D) inviscid, incompressible hydrodynamics there are two invariants of fluid motion, i.e., the total kinetic energy and the enstrophy (mean square vorticity). The existence of these two invariants requires that in the 2-D inviscid, incompressible hydrodynamics the energy cascades to the long wavelength or the vortex with the similarly signed vorticity must tend to group together.[89–93] This is analogous to the Bose–Einstein condensation of an ideal Boson gas in momentum space below the Bose–Einstein condensation temperarture.[91] Indeed, hydrodynamical experiments have shown that at the late stage of the K–H instability, two vortical structures combine to form a single, larger vortical structure.[63,65] Such vortex pairing during the nonlinear evolution of the K–H instability has been reproduced by numerical experiments of the 2-D hydrodynamics[67,71] and 2-D magnetohydrodynamics.[23,26,31]

The primary objective of the present paper is to investigate by means of a 2-D MHD simulation the basic relationship among vortex development including vortex pairing, rarefaction, and compression due to the fast magnetosonic wave, flow enhancement, eddy current, and momentum transport caused by the K–H instability in a compressible plasma, or more specifically, in a 2-D transverse configuration, where the plasma motion occurs in a plane transverse to

a)Electronic mail: miura@grl.s.u-tokyo.ac.jp

the magnetic field. The present study enables us to extend our understanding of the vortex pairing in incompressible fluids[61–69,89–93] and plasmas[23,26,31] to the 2-D compressible MHD and hydrodynamic regimes. Although there are several 2-D compressible simulations of the K–H instability in the fluid dynamics,[71–73] which show vortex pairing, the detailed relationship between the fluid rarefaction, vortex development, and flow enhancement has not been clarified in those studies. The previous 2-D MHD simulations of the K–H instability,[23,26,31] some of which have been done for different configurations including a flow parallel to the magnetic field, have not addressed the above basic issues. Furthermore, in spite of the intensive study of the K–H instability and the vortex pairing in fluids and plasmas, the relationship between the vortex pairing and the momentum transport by the Reynolds stress associated with the instability have not been fully investigated. Therefore, in order to evaluate quantitatively the momentum transport by the K–H instability with vortex pairing, the Reynolds stress by the K–H instability is measured and an anomalous viscosity by the instability is defined and measured in the present simulation.

It is well known that the 2-D inviscid, incompressible Navier–Stokes equation is identical to the 2-D guiding center description of the Vlasov equation for $k_{\|}=0$ and $k_{\perp}\rho_i \ll 1$, where $k_{\|}$ and $k_{\perp}$ are the wave numbers parallel and perpendicular to the magnetic field and ρ_i is the ion Larmor radius.[94] For compressible plasmas in the 2-D transverse configuration ($k_{\|}=0$), only the magnetic field transverse to the plasma motion is perturbed and the electric current is induced in the plane transverse to the magnetic field. Therefore, the $\mathbf{J}\times\mathbf{B}$ force in the equation of motion arises and the K–H instability in the 2-D transverse configuration[17,18,21] is slightly different from the 2-D hydrodynamical K–H instability. That is, the fast magnetosonic mode is excited[18] by the K–H instability in the 2-D compressible, transverse configuration, whereas in the 2-D compressible hydrodynamic case the sound wave is excited by the K–H instability. In other words, not only the plasma pressure but also the magnetic pressure are perturbed and responsible for the plasma motion in the 2-D compressible MHD transverse configuration.

It should be noted that at the magnetopause the momentum transport by the ion–ion Coulomb collision is neglegibly small[21] and the transport of momentum from solar wind to magnetosphere, except that due to the magnetopause reconnection, is essentially due to the anomalous transport.[95] When the thickness of the velocity shear layer at the magnetopause is smaller than or comparable to the ion Larmor radius, the anomalous transport of momentum is due to microscopic interactions.[96–100] But for the velocity shear layer with thickness larger than the ion Larmor radius, the anomalous momentum transport is essentially due to macroscopic interactions such as the MHD K–H instability. In the MHD K–H instability, both the Reynolds stress and the Maxwell stress are responsible for the anomalous transport of momentum and energy.[17,21] In the 2-D transverse configuration, however, the Maxwell stress vanishes and only the Reynolds stress caused by the K–H instability is responsible for the momentum transport.[17,21,24,28,101–103] As far as the transport of momentum and energy across the magnetopause, where the thickness of the velocity shear layer is larger than the ion Larmor radius, except near the subsolar region (where the thickness of the velocity shear layer is at times comparable to the ion Larmor radius), is concerned, it seems that a kinetic viscosity by microscopic interactions determines only ultimate dissipation of vorticity and energy at small scales, but the transport of momentum and energy itself is governed by macroscopic processes such as the K–H instability. This is analogous to the ordinary hydrodynamics, wherein the kinematic viscosity determines only the ultimate dissipation of vorticity and energy at small scales, but the transport of momentum itself is essentially due to turbulent eddies. In hydrodynamics such anomalous viscosity induced by eddies is called eddy viscosity,[104] molar viscosity,[104] or turbulent viscosity,[2] although the nature of such postulated viscosity has never been clarified and quantified, except that the postulated viscosity is due to eddies. Although in a microscopic picture the transport of momentum and energy should be described by kinetic equations, calculation and combination of the first-order velocity moments of the collisionless Boltzman equations for ions and electrons yield the momentum conservation equation or the equation of motion in the one-fluid approximation.[105] Therefore, it is not necessary to use kinetic equations for describing the momentum transport by the K–H instability, at least when the thickness of the velocity shear layer is larger than the ion Larmor radius. That is, in such a macroscale the fluid description of the perpendicular momentum transport in terms of the momentum flux or the fluid Reynolds stress is validated. This is because the locality condition of the plasma for the fluid description is well maintained in the transverse direction by the gyration of particles with a gyroradius smaller than the thickness of the velocity shear layer. Indeed, several kinetic simulations[22,27,29,32,36] of the K–H instability, assuming the velocity shear thickness equal to only a few ion Larmor radii, show that the main features of the MHD K–H instability, including the momentum transport, which have been found by the MHD simulations,[17,21] are reproduced in those kinetic simulations.

The outline of the present paper is as follows: A 2-D transverse configuration for the present 2-D MHD simulation and basic equations used in the present simulation are described and the difference between the basic equations in the 2-D MHD transverse configuration and the 2-D hydrodynamic equations is discussed by reducing the basic MHD equations for the 2-D transverse configuration to a form similar to the hydrodynamic equation in Sec. II. The enstrophy (mean square vorticity) for the 2-D transverse MHD configuration is calculated and the conservation law of the enstrophy for the compressible 2-D plasma and fluid is derived in Sec. III. The linear dispersion of the K–H instability for the 2-D MHD transverse configuration is presented for the hyperbolic tangent velocity shear profile in Sec. IV. Simulation results for the 2-D MHD transverse configuration are shown in Sec. V. Discussions and a summary are given in Sec. VI.

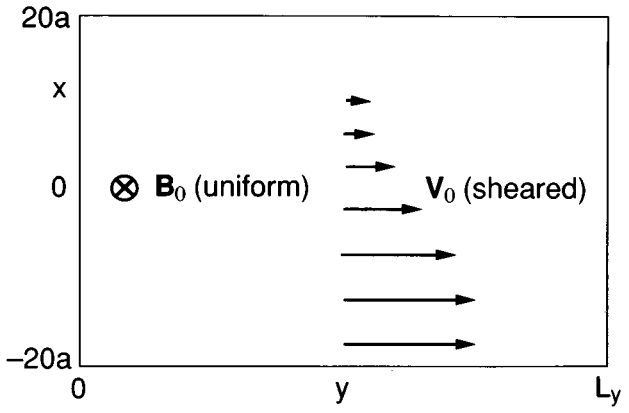

FIG. 1. The flow velocity (solid vectors) and the magnetic field in the 2-D MHD transverse configuration.

II. BASIC EQUATIONS AND 2-D MHD TRANSVERSE CONFIGURATION

The conservation equations of the ideal MHD, which describe the K–H instability, are

$$\frac{\partial \rho}{\partial t} = -\nabla \cdot (\rho \mathbf{v}), \tag{1}$$

$$\frac{\partial}{\partial t}(\rho \mathbf{v}) = -\nabla \cdot \left(\rho \mathbf{v}\mathbf{v} - \frac{1}{\mu_0}\mathbf{B}\mathbf{B} \right) - \nabla \left(p + \frac{B^2}{2\mu_0} \right), \tag{2}$$

$$\frac{\partial \mathbf{B}}{\partial t} = \nabla \times (\mathbf{v} \times \mathbf{B}), \tag{3}$$

$$\frac{\partial \epsilon}{\partial t} = -\nabla \cdot \left[\left(\epsilon + p + \frac{B^2}{2\mu_0} \right)\mathbf{v} - \frac{1}{\mu_0}(\mathbf{B}\cdot\mathbf{v})\mathbf{B} \right]. \tag{4}$$

Here, ρ, $\mathbf{v}$, $\mathbf{B}$, and p are the plasma mass density, bulk velocity of the plasma, magnetic field, and plasma pressure, and ϵ is the energy density defined by

$$\epsilon = \frac{1}{2}\rho v^2 + \frac{B^2}{2\mu_0} + \frac{p}{\Gamma - 1}, \tag{5}$$

where Γ is the ratio of specific heats.

Figure 1 shows the flow velocity and the magnetic field in a 2-D MHD transverse configuration, which is used in the following 2-D MHD simulation. A uniform background magnetic field $\mathbf{B}_0$ is transverse to the simulation plane (the x-y plane). The background plasma flow is in the y direction and the flow velocity v_y is inhomogeneous (sheared) in the x direction. The ideal MHD equations in the 2-D transverse configuration can be reduced simply to

$$\frac{d\rho}{dt} = -\rho(\nabla \cdot \mathbf{v}), \tag{6}$$

$$\rho \frac{d\mathbf{v}}{dt} = -\nabla p_t, \tag{7}$$

$$\frac{d\mathbf{B}}{dt} = -\mathbf{B}(\nabla \cdot \mathbf{v}), \tag{8}$$

$$\frac{d}{dt}(p_t \rho^{-\Gamma}) = \frac{B^2}{2\mu_0}(\Gamma - 2)\rho^{-\Gamma}(\nabla \cdot \mathbf{v}), \tag{9}$$

where p_t is the total pressure defined by $p_t = p + B^2/2\mu_0$, p being the plasma pressure, and d/dt is the total derivative equal to $\partial/\partial t + \mathbf{v}\cdot\nabla$. In deriving (6)–(9) it is only assumed that $\mathbf{B}$ is transverse to the simulation plane (i.e., $\mathbf{B}$ has the only z component) and $\mathbf{B}$ is not necessarily uniform. Note in (7) that the line bending term $(\mathbf{B}\cdot\nabla)\mathbf{B}$ in the $\mathbf{J}\times\mathbf{B}$ force in the equation of motion vanishes in the 2-D MHD transverse configuration. Since $\mathbf{B}$ has the only z component B_z, Eqs. (6) and (8) yield

$$\frac{d}{dt}\ln\left(\frac{\rho}{B_z}\right) = 0. \tag{10}$$

The equation (9) can be derived from (6), (8), and the adiabatic equation. When the plasma is incompressible ($\nabla\cdot\mathbf{v}=0$), the magnetic field and the density are not perturbed in the 2-D MHD transverse configuration and the plasma behaves like an incompressible fluid. A linear analysis for this configuration, assuming incompressibility, is given by Chandrasekhar[1] for a discontinuous velocity shear profile (the thickness of the velocity shear layer is zero). When $\Gamma = 2$, the variables ρ, $\mathbf{v}$, and p_t are governed by a closed set of Eqs. (6), (7), and (9), and the magnetic field does not appear explicitly in the closed equations. Therefore, as far as the evolution of ρ, $\mathbf{v}$, and p_t in the 2-D MHD transverse configuration is concerned, the plasma behaves like a 2-D adiabatic pseudofluid with the gas pressure replaced by the total pressure p_t. Therefore, in such a case, the dynamics of the K–H instability is not essentially different from the 2-D hydrodynamic K–H instability. When the plasma is compressible and $\Gamma \neq 2$, however, B_z appears explicitly in the governing equations [Eq. (9)], and there is essentially a difference between the K–H instability in the 2-D MHD transverse configuration and the K–H instability in the 2-D hydrodynamic configuration. In the 2-D MHD transverse configuration used in the following simulation it is assumed that the initial magnetic field $\mathbf{B_0}$ in the positive z direction is uniform, $\partial/\partial z = 0$, the initial density ρ_0 is uniform, and the ratio of specific heats Γ is equal to $\frac{5}{3}$. Since ρ/B_z is initially uniform in the following 2-D MHD transverse configuration, ρ/B_z is an invariant of the plasma motion according to (10), that is, ρ and B_z remain proportional. Although the simulation results only for $\Gamma = \frac{5}{3}$ are presented in Sec. V, it is found that the results of the MHD simulation are rather insensitive to the choice of Γ, as described in detail in Sec. VI.

III. ENSTROPHY AND INVERSE ENERGY CASCADE

In the 2-D inviscid, incompressible hydrodynamic flow, the total kinetic energy and the enstrophy (mean square vorticity) are two invariants of the fluid motion.[89–93] Since the conservation law of the enstrophy for the compressible plasma (or, more generally, fluid) is not trivial and its derivation from the equation of motion cannot be found elsewhere, the conservation law of the enstrophy for the 2-D compressible plasma in the 2-D MHD transverse configuration or the 2-D compressible fluid is derived in the following.

The equation (7) can be written as

$$\rho\left(\frac{\partial \mathbf{v}}{\partial t}+(\mathbf{v}\cdot\nabla)\mathbf{v}\right)=-\nabla p_t. \tag{11}$$

Taking the curl of this equation, we obtain

$$\frac{\partial}{\partial t}(\nabla\times\mathbf{v})+\nabla\times[(\mathbf{v}\cdot\nabla)\mathbf{v}]=\frac{\nabla\rho\times\nabla p_t}{\rho^2}, \tag{12}$$

where the vector product on the right-hand side (rhs) $\nabla\rho\times\nabla p_t/\rho^2$ is the baroclinic vector. Using the vector identity,

$$(\mathbf{v}\cdot\nabla)\mathbf{v}=\tfrac{1}{2}\nabla(\mathbf{v}^2)-\mathbf{v}\times(\nabla\times\mathbf{v}), \tag{13}$$

we obtain from (12),

$$\frac{\partial}{\partial t}(\nabla\times\mathbf{v})-\nabla\times[\mathbf{v}\times(\nabla\times\mathbf{v})]=\frac{\nabla\rho\times\nabla p_t}{\rho^2}. \tag{14}$$

By expanding the second term on the left-hand side (lhs), we obtain

$$\frac{\partial}{\partial t}(\nabla\times\mathbf{v})+(\nabla\times\mathbf{v})(\nabla\cdot\mathbf{v})-[(\nabla\times\mathbf{v})\cdot\nabla]\mathbf{v}+(\mathbf{v}\cdot\nabla)(\nabla\times\mathbf{v})=\frac{\nabla\rho\times\nabla p_t}{\rho^2}. \tag{15}$$

In the 2-D transverse configuration, where $\mathbf{v}=v_x(x,y)\hat{\mathbf{x}}+v_y(x,y)\hat{\mathbf{y}}$ and $\partial/\partial z=0$, we have

$$[(\nabla\times\mathbf{v})\cdot\nabla]\mathbf{v}=0. \tag{16}$$

Therefore, (15) can be reduced to

$$\frac{\partial}{\partial t}(\nabla\times\mathbf{v})+(\nabla\times\mathbf{v})(\nabla\cdot\mathbf{v})+(\mathbf{v}\cdot\nabla)(\nabla\times\mathbf{v})=\frac{\nabla\rho\times\nabla p_t}{\rho^2}. \tag{17}$$

Taking the scalar product of (17) and $\nabla\times\mathbf{v}$ and using the vector identities

$$(\nabla\times\mathbf{v})^2(\nabla\cdot\mathbf{v})=\nabla\cdot[\mathbf{v}(\nabla\times\mathbf{v})^2]-(\mathbf{v}\cdot\nabla)(\nabla\times\mathbf{v})^2, \tag{18}$$

and

$$(\nabla\times\mathbf{v})\cdot[(\mathbf{v}\cdot\nabla)(\nabla\times\mathbf{v})]=\tfrac{1}{2}(\mathbf{v}\cdot\nabla)(\nabla\times\mathbf{v})^2, \tag{19}$$

we obtain from (17),

$$\frac{\partial}{\partial t}(\nabla\times\mathbf{v})^2+\nabla\cdot[\mathbf{v}(\nabla\times\mathbf{v})^2]+(\nabla\times\mathbf{v})^2(\nabla\cdot\mathbf{v})=2(\nabla\times\mathbf{v})\cdot\frac{(\nabla\rho\times\nabla p_t)}{\rho^2}. \tag{20}$$

Let us take a volume V, which consists of a region with $-x_b\leqslant x\leqslant x_b$, $0\leqslant y\leqslant L_y$, and $0\leqslant z\leqslant 1.0$, and a surface A surrounding the volume V. By taking the volume integral of (20), we obtain

$$\frac{\partial}{\partial t}\int\int\int_V dV(\nabla\times\mathbf{v})^2+\int\int\int_V dV\,\nabla\cdot[\mathbf{v}(\nabla\times\mathbf{v})^2]+\int\int\int_V dV(\nabla\times\mathbf{v})^2(\nabla\cdot\mathbf{v})=\int\int\int_V dV\,2(\nabla\times\mathbf{v})\cdot\frac{(\nabla\rho\times\nabla p_t)}{\rho^2}. \tag{21}$$

Using Gauss' theorem, the second term on the lhs can be replaced by a surface integral, i.e.,

$$\int\int\int_V dV\,\nabla\cdot[\mathbf{v}(\nabla\times\mathbf{v})^2]=\int\int_A d\mathbf{S}\cdot[\mathbf{v}(\nabla\times\mathbf{v})^2]. \tag{22}$$

As is assumed in the following 2-D MHD simulation, let us assume that $\mathbf{v}$ is periodic in the y direction, i.e., $\mathbf{v}(x,y=0)=\mathbf{v}(x,y=L_y)$, $v_x=0$ at boundaries in the x direction at $x=\pm x_b$, and $\mathbf{v}$ is independent of z. Then, (22) is identically zero. Therefore, we obtain from (21),

$$\frac{\partial}{\partial t}\int\int_C dx\,dy(\nabla\times\mathbf{v})^2=-\int\int_C dx\,dy(\nabla\times\mathbf{v})^2(\nabla\cdot\mathbf{v})+\int\int_C dx\,dy\,2(\nabla\times\mathbf{v})\cdot\frac{(\nabla\rho\times\nabla p_t)}{\rho^2}, \tag{23}$$

where the lhs is proportional to the time derivative of the enstrophy (mean square vorticity) and C represents a region in the x-y plane with $-x_b\leqslant x\leqslant x_b$ and $0\leqslant y\leqslant L_y$. This gives the conservation law of the enstrophy in C. In the present 2-D transverse configuration, where ρ_0 and $\mathbf{B}_0$ are uniform, ρ and B_z remain proportional. Therefore, the baroclinic vector $\nabla\rho\times\nabla p_t/\rho^2$ is equal to $\nabla\rho\times\nabla p/\rho^2$, which is the same as the baroclinic vector in the hydrodynamic case. If the plasma (fluid) is uniform initially and incompressible ($\nabla\cdot\mathbf{v}=0$), the density ρ is not perturbed [see (6)] and $\nabla\rho=0$. Therefore, we recover from (23) that in the 2-D uniform, incompressible plasma (fluid) the enstrophy is an invariant of the plasma (fluid) motion. In a more general case, where either the plasma (fluid) is compressible or the baroclinic vector is nonzero, the enstrophy is not an invariant of the 2-D plasma (fluid) motion.

In the 2-D transverse configuration ($\mathbf{B}\perp\mathbf{v}$), taking the volume integral of the energy conservation equation (4) and using the boundary condition lead to

$$\frac{\partial}{\partial t}\int\int_C dx\,dy\left(\frac{1}{2}\rho v^2+\frac{B^2}{2\mu_0}+\frac{p}{\Gamma-1}\right)=0. \tag{24}$$

This is the conservation law of the total energy in the C region. In the uniform, incompressible case ($\Gamma\to\infty$), B_z and ρ are not perturbed and $\rho=\rho_0$. Therefore,

$$\frac{\partial}{\partial t}\int\int_C dx\,dy\,v^2=0. \tag{25}$$

That is, the total kinetic energy or the mean square velocity is an invariant. The existence of the two invariants, i.e., the total kinetic energy and the enstrophy, in the 2-D incompressible hydrodynamic case with a uniform density, and in the present 2-D incompressible MHD transverse case leads to a consequence[89–93] that the bulk of the energy concentrates in the small wave numbers (inverse energy cascade); in other words, the fluid elements with similarly signed vorticity must tend to group together. The inverse energy cascade or the tendency for the bulk of energy to concentrate in the

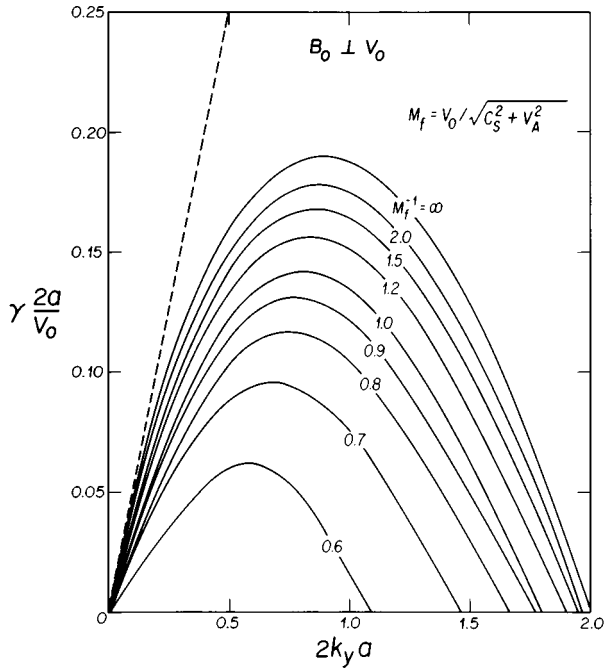

FIG. 2. The normalized linear growth rate versus the normalized wave number. Here M_f is the magnetosonic Mach number defined by $M_f = V_0/\sqrt{C_S^2+V_A^2}$. The dashed line is the growth rate for the discontinuous velocity profile in the incompressible case.

small wave numbers is verified for a 2-D MHD transverse configuration, where the compressibility is small and $\nabla\rho$ is parallel to ∇p_t in the following simulation. In general, for a compressible 2-D MHD transverse configuration or 2-D fluid, the conservation equations are (23), (24), and (10) (for MHD only), and the inverse energy cascade cannot be proven mathematically.

IV. LINEAR DISPERSION

In the following, 2-D MHD simulations are performed in the x-y plane perpendicular to the magnetic field. The initial flow velocity v_{0_y} has a shear profile,

$$v_{0_y}(x) = V_0/2[1-\tanh(x/a)], \tag{26}$$

and the other equilibrium quantities (B_0, p_0, ρ_0) are uniform. We impose a boundary condition such that there is no mass flow $(v_x = 0)$ across the boundaries at $x = \pm x_b = \pm 20a$, and all quantities are periodic in the y direction.[17,21] A linear eigenmode analysis for the plasma configuration with a velocity shear profile (26) has been performed to obtain the linear growth rate as a function of the wave number and Mach numbers. Since the detailed calculation of the linear dispersion of the MHD K–H instability for this configuration is reported elsewhere,[18] only a brief summary of the results is given here.

Since the real frequency of the K–H instability is due to the Doppler shift due to the mean bulk flow, the dispersion relation gives $\omega_r = k_y V_0/2$, where ω_r is the real part of the angular frequency. Figure 2 shows normalized growth rates γ of the K–H instability for the 2-D transverse configuration shown in Fig. 1 and $k_z = 0$ as a function of the normalized wave number $(2k_y a)$. The growth rate is normalized by $V_0/2a$, and the wave number is normalized by $(2a)^{-1}$. Note that only the fast magnetosonic mode is destabilized in the 2-D transverse configuration of the K–H instability. Therefore, the appropriate Mach number for the background flow is the fast magnetosonic Mach number defined by $M_f = V_0/\sqrt{C_S^2+V_A^2}$, where $V_A = B_0/(\mu_0\rho_0)^{1/2}$ and $C_S = (\Gamma p_0/\rho_0)^{1/2}$. Notice that an important Mach number, which characterizes the intrinsic compressibility of the flow, is the convective Mach number[70] $M_{fc} = M_f/2$, which is the Mach number in a frame of reference comoving with the phase velocity of the unstable K–H wave. The dashed line represents the growth rate $\gamma = k_y V_0/2$ obtained analytically for the incompressible transverse configuration with a zero thickness of the velocity shear layer.[1] Clearly, this result is valid only when the thickness of the velocity shear layer $2a$ is much smaller than the wavelength in the y direction, i.e., $2k_y a \ll 1.0$. The uppermost solid curve $(M_f^{-1} = \infty)$ represents the growth rate obtained numerically in the incompressible case. This curve was taken from a numerical calculation of Michalke.[106] The growth rate for the incompressible case reaches a maximum for $2k_y a \sim 0.9$ and then decreases with increasing $2k_y a$, reaching zero for $2k_y a = 2.0$. As the Mach number M_f increases from zero (and hence the compressibility becomes important), the normalized growth rate is reduced considerably. In addition, the wave number of the fastest growing mode, k_{FGM}, and the critical wave number beyond which the mode is completely stabilized, $k_{y\mathrm{cr}}$, are shifted toward smaller values with increasing M_f. This figure shows how the compressibility stabilizes the K–H instability with an increasing M_f. The fastest growing mode always appears at the wave number satisfying $0.5 < 2k_y a < 1.0$. Consequently, the fastest growing mode has a wavelength of the order of $2\pi \times 2a \sim 4\pi \times 2a$, which is characterized by the finite thickness of the velocity shear layer $(2a)$.

V. SIMULATION RESULTS

Physical parameters used in the present simulation are the sound Mach number $M_S = V_0/C_S = 1.0$ and the Alfvén Mach number $M_A = V_0/V_A = 1.0$. The fast mode Mach number M_f is $M_f = 0.71$ and the convective fast magnetosonic Mach number is $M_{fc} = 0.35$. We use a time T normalized by $2a/V_0$. Figure 2 shows that for this configuration, the linearly fastest growing mode occurs at $2k_y a \sim 0.8$, with its growth rate equal to $0.17V_0/2a$. Therefore, the wavelength of the linearly fastest growing mode λ_{FGM} is equal to $15.7a$. The length L_y of the simulation system in the y direction is chosen equal to $4 \cdot \lambda_{\mathrm{FGM}} = 62.8a$. Since the present simulation is a MHD simulation, it is necessary to give explicitly an initial seed perturbation at $T = 0$. In the present simulation a superposition of the approximate linear eigenfunction of the fastest growing mode in the incompressible case[13,101] and its subharmonic modes is added to the equilibrium at $T = 0$ as an initial seed perturbation. The peak amplitude of the initial flow velocity perturbation is $0.005V_0$. The explicit form of the seed perturbation is as follows:

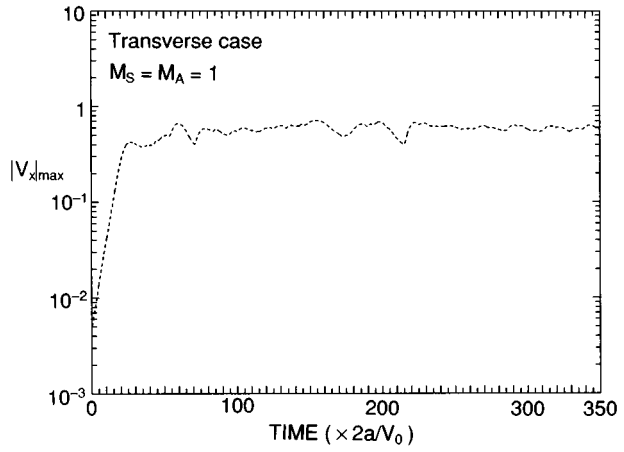

FIG. 3. Temporal evolution of the peak of the x component of the flow velocity $|v_x|_{\max}$ normalized by V_0 as a function of the normalized time.

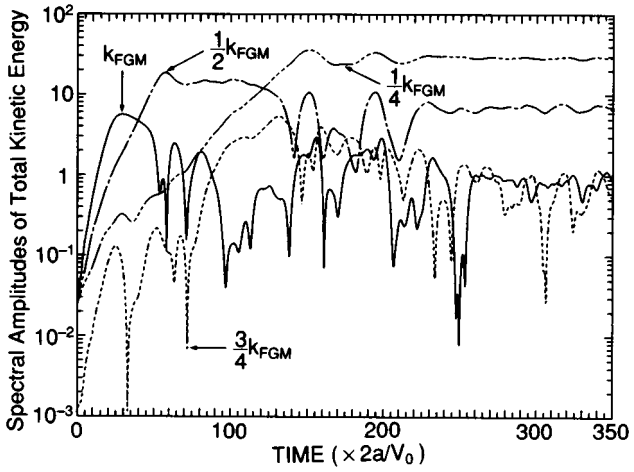

FIG. 4. Temporal evolution of the amplitudes of the fundamental mode with $k=k_{\mathrm{FGM}}$ (solid curve), the first subharmonic with $k=k_{\mathrm{FGM}}/2$ (dot–dashed curve), the second subharmonic with $k=k_{\mathrm{FGM}}/4$ (triple dot–dashed curve), and the Fourier mode with $k=3k_{\mathrm{FGM}}/4$ (dotted curve) of the total kinetic energy integrated along x. All amplitudes are normalized by $2ap_0$.

$$v_x(x,y)=\sum_{n=1,3} 2k_n[-\phi_r(x)\sin(k_n y)-\phi_i(x)\cos(k_n y)], \tag{27}$$

$$v_y(x,y)=-\sum_{n=1,3} 2\left(\frac{d\phi_r(x)}{dx}\cos(k_n y) - \frac{d\phi_i(x)}{dx}\sin(k_n y)\right), \tag{28}$$

where

$$k_n=k_{\mathrm{FGM}}/2^{n-1}=(0.8/2a)/2^{n-1} \quad (n=1,2,3), \tag{29}$$

$$\phi_r(x)=\Psi_0\ \exp\left(-\frac{x^2}{a^2}\right)\cos\left[\frac{\pi}{2}\sin\left(\frac{\pi x}{2a}\right)\right], \tag{30}$$

$$\phi_i(x)=\Psi_0\ \exp\left(-\frac{x^2}{a^2}\right)\sin\left[\frac{\pi}{2}\,\sigma\,\sin\left(\frac{\pi x}{2a}\right)\right]. \tag{31}$$

Here Ψ_0 is the arbitrary constant to determine the amplitude of the initial perturbation and σ determines the inclination of the vortex with respect to the mean flow, which determines whether the vortex is growing or decaying.[101] That is, $\sigma=-1$ for the growing vortex and $\sigma=1$ for the decaying vortex. In solving the conservation equations of the ideal MHD (1)–(4), the two-step Lax–Wendroff scheme is used and the number of grids is equal to 200×200.

Figure 3 shows temporal evolution of the peak of the x component of the flow velocity $|v_x|_{\max}$ normalized by V_0 as a function of time. In the initial stage from $T=0$ to $T\sim20$, the peak of $|v_x|_{\max}$ increases exponentially with a linear growth rate $\sim0.19V_0/2a$, which is comparable to the predicted linear growth rate of the fastest growing mode. This means that the initial seed perturbation specified by (27)–(31) is very close to the exact unstable eigenfunction. At $T\sim30$, the peak velocity levels off and after $T\sim30$ the peak amplitude is susceptible to a small but finite-amplitude oscillation associated with a vortex nutation.[61,101,103] It is seen in this figure that the peak amplitude increases slightly with time until $T\sim200$ after $T\sim30$. This slight increase of the peak amplitude is due to the growth of the subharmonic modes.

Figure 4 shows temporal evolution of the Fourier amplitudes of the fastest growing mode (fundamental mode) and its subharmonics of the total kinetic energy in the simulation region, which is integrated along x. The four modes have the wave numbers k equal to $k_{\mathrm{FGM}}/4$, $k_{\mathrm{FGM}}/2$, $3k_{\mathrm{FGM}}/4$, and k_{FGM}, where k_{FGM} is the wave number of the fastest growing mode. Each mode amplitude is normalized by $2ap_0$. At $T=0$ three modes with $k=k_{\mathrm{FGM}}$ (fundamental), $k_{\mathrm{FGM}}/2$ (first subharmonic), and $k_{\mathrm{FGM}}/4$ (second subharmonic) have the same amplitudes as a consequence of the specification of the initial seed perturbation by (27) and (28). Those three modes grow linearly in their linear phases. The growth rates of those modes were calculated from their linear slopes in the initial growth phases. The calculated growth rates are $0.19V_0/2a$, $0.104V_0/2a$, $0.0532V_0/2a$ for the fundamental (solid curve), the first subharmonic (dot–dashed curve), and the second subharmonic (triple dot–dashed curve), respectively. Figure 2 shows that growth rates obtained theoretically for these three modes are $0.17V_0/2a$, $0.12V_0/2a$, and $0.065V_0/2a$, respectively. Although the observed growth rates for subharmonics are slightly smaller than the predicted linear growth rates, there is good agreement between the predicted linear growth rates and the linear growth rates obtained from the simulation run. The fundamental mode, the first subharmonic, and the second subharmonic reach their peak amplitudes at $T\sim30$, $T\sim55$, and $T\sim150$, respectively. Although the fundamental mode has the largest growth rate, the second subharmonic reaches the largest amplitude during the simulation run. It should be noted that a clear finite-amplitude amplitude oscillation is seen for the second subharmonic from $T=150$ to $T=220$, although it disappears after $T\sim230$, owing to the phase mixing among its higher harmonics. This amplitude oscillation of the second subharmonic is similar in nature to the amplitude oscillation of the fundamental mode, which is found when the growth of subharmonics is inhibited.[101,103]

Figure 5 shows contour lines of the z component of the

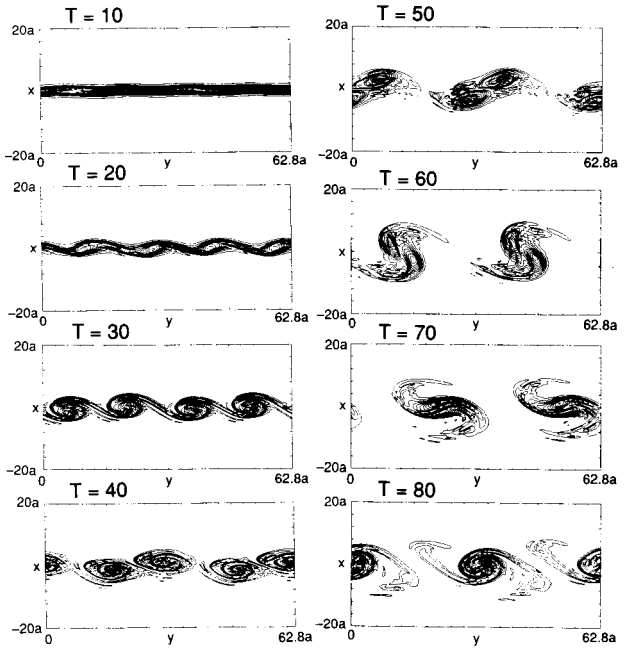

FIG. 5. Contour lines of the z component of the vorticity at eight different times from $T=10$ to $T=80$. In all panels the contour lines are plotted for negative vorticity (counterclockwise rotation).

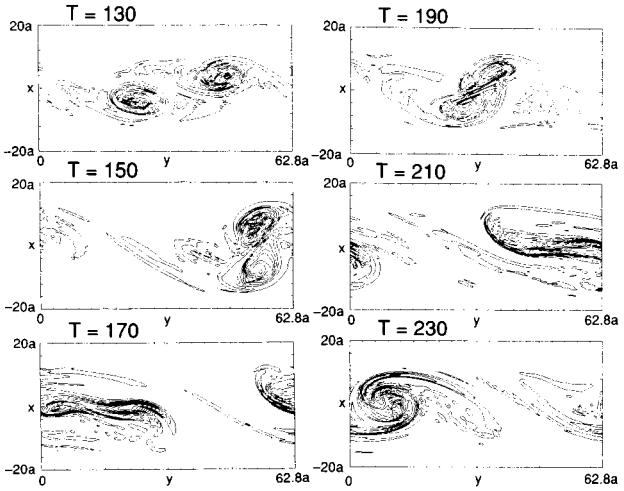

FIG. 6. Contour lines of the z component of the vorticity at six different times from $T=130$ to $T=230$. In all panels the contour lines are plotted for negative vorticity (counterclockwise rotation).

vorticity Ω_z at eight different times from $T=10$ to $T=80$. In the 2-D transverse configuration, Ω_z is calculated from the frozen-in law as

$$\Omega_z=\hat{\mathbf{z}}\cdot(\nabla\times\mathbf{v})=-\frac{1}{B}\nabla\cdot\mathbf{E}+\frac{\mu_0}{B}(\mathbf{J}\cdot\mathbf{v}_\perp), \tag{32}$$

where $\mathbf{E}$ is the electric field satisfying the frozen-in law and $\mathbf{J}$ is the electric current density. This shows that in the 2-D incompressible plasma, where $\mathbf{B}$ is not perturbed and $\mathbf{J}$ is zero, the vorticity is proportional to the space charge density. In all panels the contour lines are plotted for negative vorticity (counterclockwise rotation). In the early phase an initial straight vorticity layer (velocity shear layer) undulates ($T=10$) and it develops into a vortex train at $T=30$. Four vortices appear as predicted by the linear theory. Note that the fundamental Fourier mode of the total kinetic energy reaches its peak amplitude at $T=30$ (see Fig. 4). At $T=40$, two neighboring vortices begin to rotate around each other. At $T=50$, two neighboring vortices begin to merge shortly before $T\sim55$, when the first subharmonic reaches its peak amplitude (see Fig. 4). Each vortex rotates counterclockwise around each other and at $T=80$ two vortices are formed out of the initial four vortices as a consequence of the vortex pairing (coalescence of vortices). This process of the vortex pairing is very similar to that reported in the hydrodynamics.[63,65,71–73]

Figure 6 shows contour lines of the vorticity Ω_z at six different times from $T=130$ to 230. At $T=130$ again, the two neighboring vortices begin to rotate counterclockwise around each other and the two vortices begin to merge at $T=150$, when the second subharmonic reaches its peak amplitude (see Fig. 4). The vorticity is stretched in the y direction at $T=170$ and $T=210$. After a few rotations around each other the two vortices coalesce to form a single large vortex at $T=230$.

Figure 7 shows, from the top, contour lines of pressure, flow velocity vectors, and current vectors at $T=40$. The pressure is normalized by the initial uniform pressure p_0 and the velocity vectors are normalized by V_0. By $T=40$, the linearly fastest growing mode has developed fully into the nonlinear stage and four pairs of a low-pressure (rarefied) region and a high-pressure (compressed) region line up near $x\sim0$. Figure 7(a) shows that at the bottom of the low-pressure region (denoted by L), the pressure becomes $0.776p_0$ and at the peak of the high-pressure region (denoted by H), the peak pressure reaches $1.14p_0$. The rarefied region has a much steeper pressure gradient than in the compressed region. The B_z component is reduced in the low-pressure region as well, and it is enhanced in the high-pressure region, because only the fast magnetosonic mode with the change of the magnetic pressure in phase with the thermal pressure is excited by the instability in the 2-D MHD transverse configuration.[18] Figure 7(b) shows that four vortices rotating counterclockwise have developed near $x=0$ by $T=40$. Note that the vortical flow appears only in the rarefied region in Fig. 7(a). Figure 7(c) shows that the eddy current flowing counterclockwise is associated with each vortex in Fig. 7(b). The electric current $\mathbf{J}_\perp$ is calculated from the equation of motion as

$$\mathbf{J}_\perp=\rho\frac{\mathbf{B}}{B^2}\times\frac{d\mathbf{v}}{dt}+\frac{\mathbf{B}}{B^2}\times\nabla p. \tag{33}$$

Since the direction of $\mathbf{B}\times\nabla p$ is clockwise in the rarefied region and thus opposite to the direction of the observed eddy current, the eddy current observed in the rarefied region, associated with each flow vortex, must be the inertia current [the first term on the rhs of (33)] in nature. In other words, the centrifugal force by the counterclockwise rotation, which is responsible for expelling the plasma outward

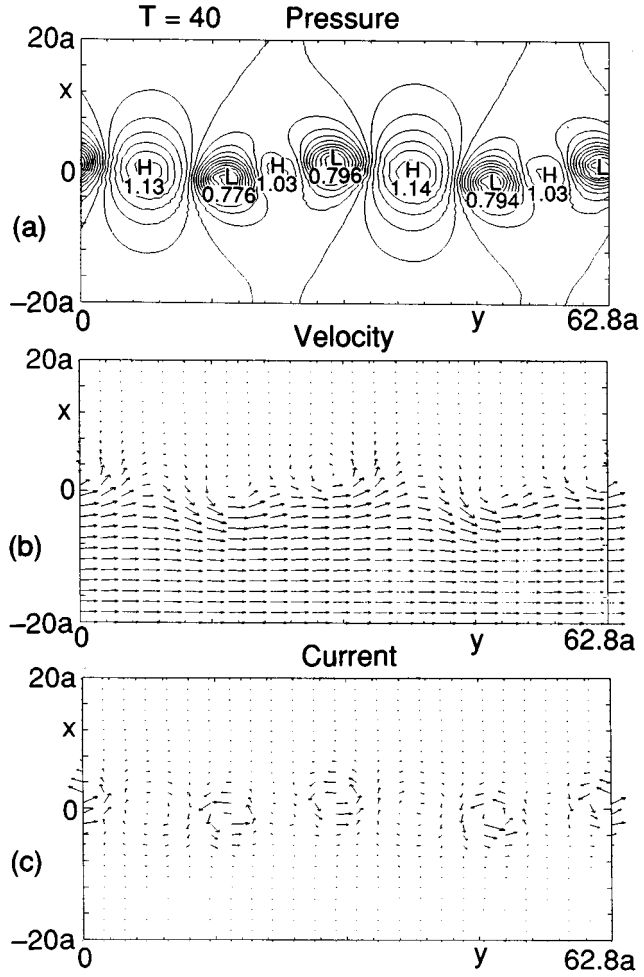

FIG. 7. (a) Contour lines of pressure, (b) flow velocity vectors, and (c) current vectors at $T=40$. Here H and L in (a) represent the positions of maximum and minimum pressures, respectively. In (a) the maximum and minimum values of the pressure normalized by p_0 are shown by numbers.

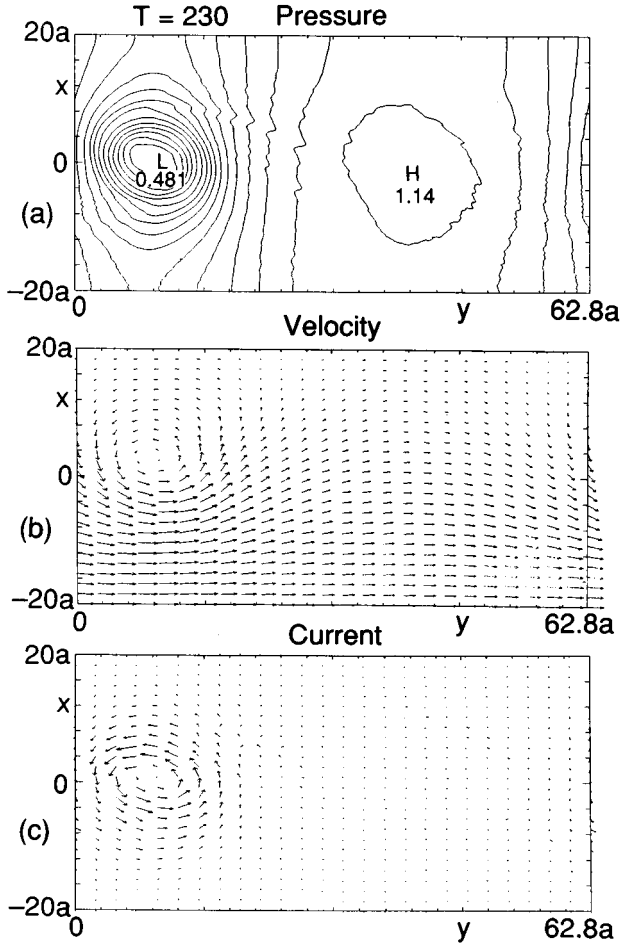

FIG. 8. (a) Contour lines of pressure, (b) flow velocity vectors, and (c) current vectors at $T=230$. Here H and L in (a) represent the positions of maximum and minimum pressures, respectively. In (a) the maximum and minimum values of the pressure normalized by p_0 are shown by numbers.

from inside the vortex, is balanced by the sum of the $\mathbf{J}\times\mathbf{B}$ force and the $-\nabla p$ force directed to the center of the vortex.

Figure 8 shows, from the top, contour lines of pressure, flow velocity vectors, and current vectors at $T=230$. Figure 8(a) shows that a pair of low- and high-pressure regions develops after the second vortex pairing at $T=230$. In the low-pressure region the minimum pressure (denoted by L) becomes as low as $0.481p_0$, owing to a strong fast rarefaction (rarefaction due to the fast magnetosonic mode excited by the instability), and in the high-pressure region the peak of the pressure (denoted by H) reaches $1.14p_0$. As is true at $T=40$ [Fig. 7(a)], the pressure gradient is much stronger in the rarefied region than in the compressed region. In the rarefied region a large vortex rotating counterclockwise develops [Fig. 8(b)]. Figure 8(b) also shows that in the compressed region between vortices, the large flow momentum in the y direction in $x<0$ is transported to $x>0$. As is described in more detail in Figs. 10 and 11, it is seen in Fig. 7(b) and Fig. 8(b) that the flow velocity is enhanced or the plasma is accelerated at the periphery of the vortex in $x<0$ at $T=40$ and 230. The flow enhancement is stronger at $T=230$ than at $T=40$. Figure 8(c) shows that a large isolated eddy current due to the inertia current develops in the low-pressure region in association with the large isolated vortical flow.

Figure 9(a) shows contour lines of the plasma density at $T=230$, which is normalized by the initial density ρ_0. The equation (10) shows that in the 2-D transverse configuration the plasma density ρ and B_z remain proportional. Therefore, this panel also shows contour lines of B_z normalized by the initial uniform magnetic field B_0 at $T=230$. At the bottom of the low-density region (denoted by L) the density becomes as low as $0.64\rho_0$, where ρ_0 is the initial uniform density, and at the peak of the high-density region (denoted by H), the peak density reaches $1.07\rho_0$. The low-density region located at the flow vortex has a much steeper density gradient than in the high-density region. Figure 9(b) shows contour lines of the plasma temperature T_p normalized by the initial uniform temperature T_0 at $T=230$. At the bottom of the low-temperature region (denoted by L) the temperature becomes $0.747T_0$. At the peak of the high-temperature region (denoted by H), the peak temperature reaches $1.07T_0$. Therefore, the adiabatic cooling of the plasma occurs inside the flow vortex and the adiabatic heating occurs between vortices. The low-temperature region located at the isolated flow

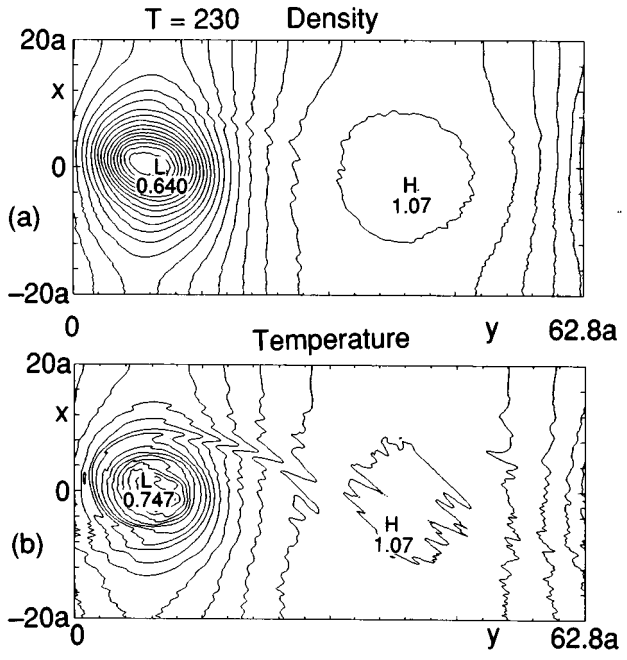

FIG. 9. Contour lines of (a) density and (b) temperature at $T=230$. Here H and L in (a) and (b) represent the positions of maximums and minimums of (a) density and (b) temperature. The maximum and minimum values of (a) the density and (b) the temperature normalized by ρ_0 and T_0, respectively, are shown by numbers.

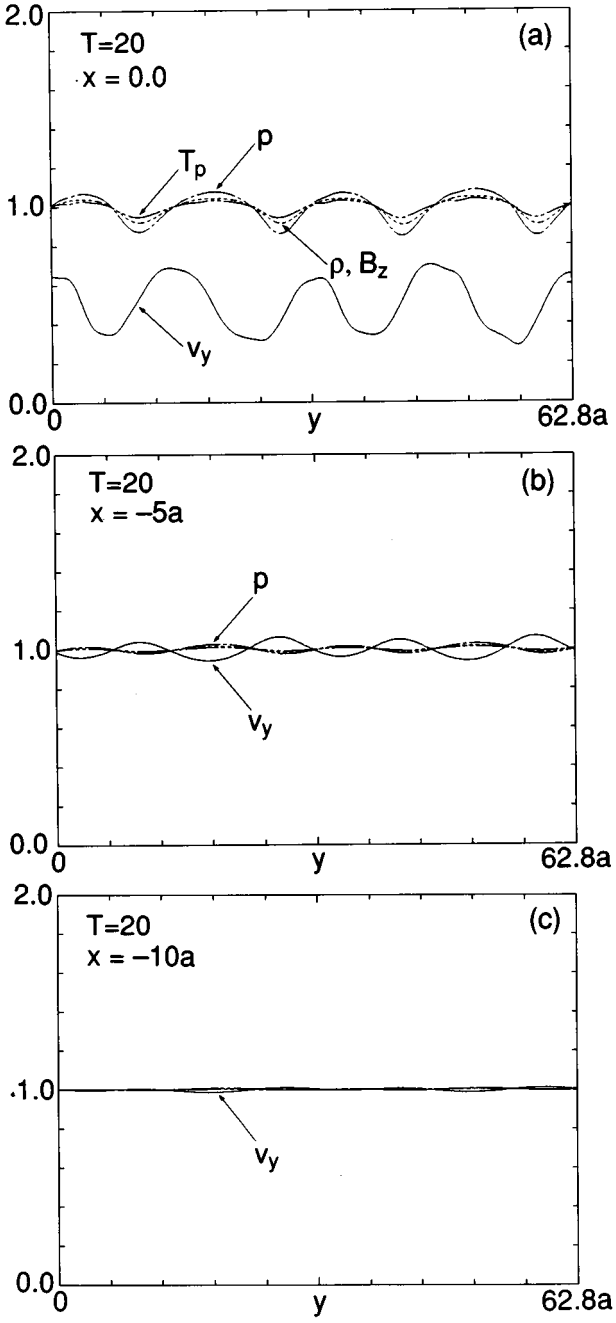

FIG. 10. Profiles in the y direction of pressure p (dot–dashed curve) normalized by P_0, temperature T_p (double dot–dashed curve) normalized by T_0, density ρ (dashed curve) normalized by ρ_0, and the y component of the velocity v_y (solid curve) normalized by V_0 at (a) $x=0$, (b) $x=-5a$, (c) $x=-10a$, and at $T=20$.

vortex has a much steeper temperature gradient than in the high-temperature region.

Figure 10(a) shows profiles in the y direction of pressure p (dot–dashed curve) normalized by p_0, temperature T_p (double dot-dashed curve) normalized by T_0, density ρ (dashed curve) normalized by ρ_0, and the y component of the velocity v_y (solid curve) normalized by V_0 at $x=0$ and at $T=20$, when the perturbation is still growing linearly (see Fig. 3). Note that at $T=20$ the fundamental mode is still growing linearly before it levels off at $T\sim 30$ (see Fig. 4). The equation (10) shows that the density and B_z remain proportional. Therefore, the profile of the normalized B_z is the same as the profile of the normalized density ρ. As is obvious from this panel, normalized p, ρ, B_z, and T_p become less than 1.0, which is their original value at $T=0$, at their minima inside the vortex, owing to a rarefaction due to the fast magnetosonic wave excited by the instability, but they become slightly larger than 1.0 at their peaks, owing to a compression due to the fast magnetosonic wave excited by the instability. As is predicted by the linear theory, four minima and four peaks of p, ρ, B_z, and T_p appear in the simulation box in the linear phase at $T=20$. The velocity component v_y at $x=0$ undulates, owing to a development of vortices, and there is about $\pi/2$ phase difference between the peaks of p, ρ, B_z, and T_p and the peak of v_y. Figure 10(b) shows the same profiles as in Fig. 10(a) at $T=20$ and at $x=-5a$. The periodic rarefaction and compression of the plasma are seen in this panel as well. The profile of v_y and those of p, ρ, B_z, and T_p have an almost out of phase relationship (a phase difference of π). That is, where the p, ρ, B_z, and T_p have minima, v_y has a peak larger than 1.0. Since the peak of the initial v_y is 1.0, this means that there is a slight acceleration of plasma or enhancement of the flow velocity, preferentially in the y direction at $x=-5a$, where the plasma is rarefied. Figure 10(c) shows the same profiles as in Fig. 10(a) at $T=20$ and at $x=-10a$. All quantities remain almost the same as their initial values. This means that the periphery of the vortices excited by the instability has not yet reached $x=-10a$ by this time.

Figure 11(a) shows the same profiles as in Fig. 10 at $x=0$ and at $T=230$, when the four vortices have merged to

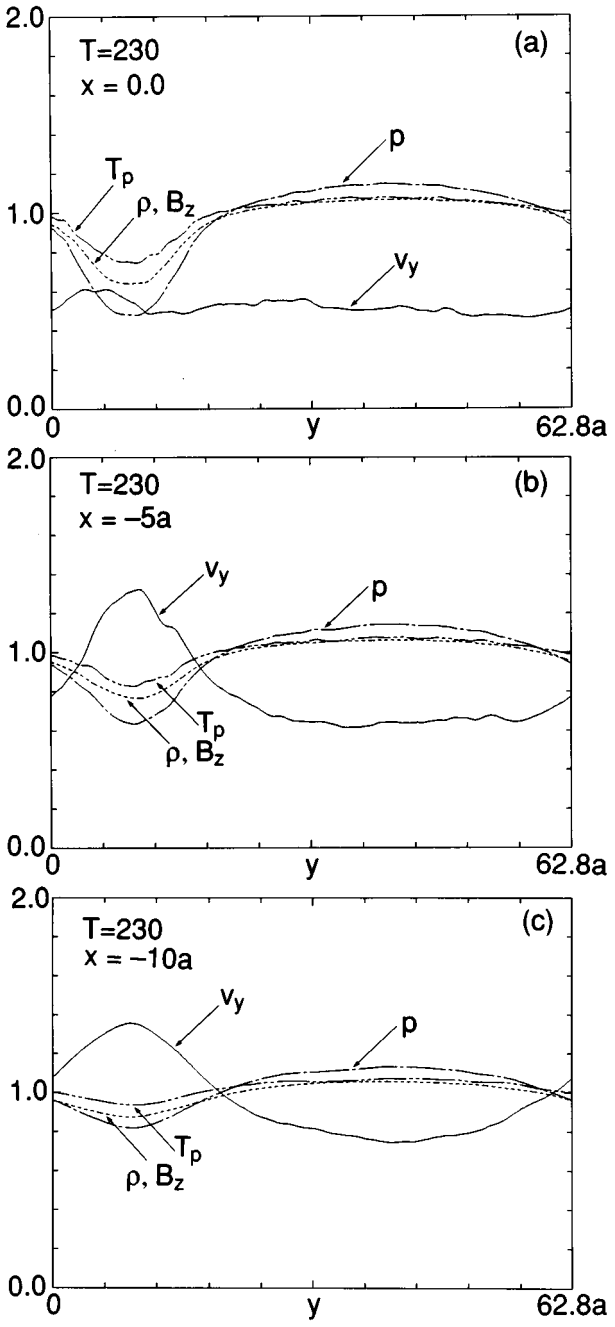

FIG. 11. Profiles in the y direction of pressure p (dot–dashed curve) normalized by p_0, temperature T_p (double dot–dashed curve) normalized by T_0, density ρ (dashed curve) normalized by ρ_0, and the y component of the velocity v_y (solid curve) normalized by V_0 at (a) $x=0$, (b) $x=-5a$, (c) $x=-10a$, and at $T=230$.

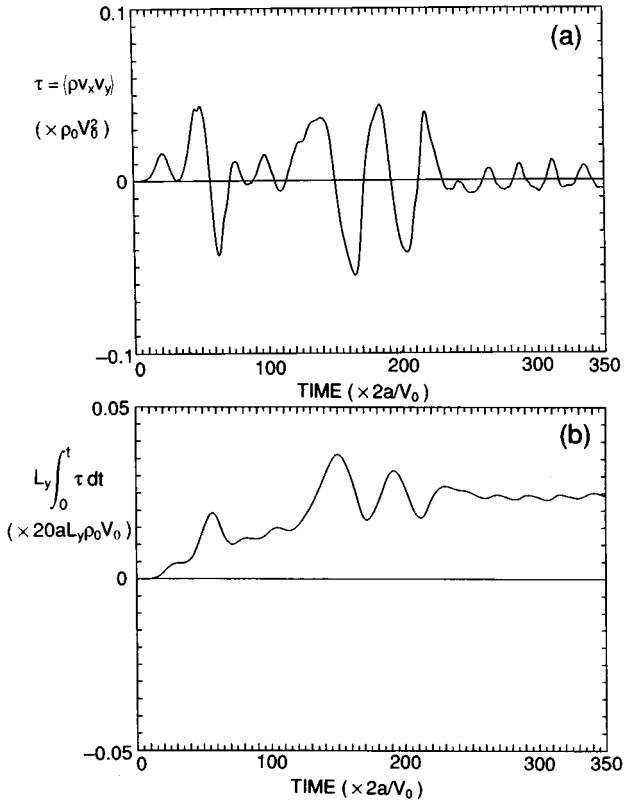

FIG. 12. (a) Temporal evolution of the normalized Reynolds stress at $x=0$ averaged over the y direction (upper panel) and (b) temporal evolution of the normalized time integral of the averaged tangential stress at $x=0$, which is equal to the total flow momentum in the positive y direction in $x>0$.

form a single isolated large vortex. At this time, p, ρ, B_z, and T_p have deep minima at $y\sim 10a$ and they have broad peaks near $y\sim 40a$. The normalized pressure p becomes less than half of the original value (1.0) at $y\sim 10a$ due to the fast magnetosonic rarefaction. The temperature also decreases considerably within this rarefied region located inside the vortex, owing to an adiabatic cooling. Originally the normalized velocity component v_y is equal to 0.5 at $x=0$, but it is slightly accelerated inside the vortex and is nearly equal to 0.6 at $T=230$. As we have seen in Fig. 10, there is a phase difference between the minima of p, ρ, B_z, and T_p and the maximum of v_y. Figure 11(b) shows the same profiles as in Fig. 10 at $T=230$ and at $x=-5a$, which is off the vortex center. Here, p, ρ, B_z, and T_p have minima inside the vortex at $y\sim 10a$ and they have broad maxima at $y\sim 40a$. Inside the vortex the flow component v_y is strongly accelerated locally and it exceeds 1.0, which was equal to the original peak flow velocity in the simulation box. Figure 8(b) shows that at the maximum of v_y, there is also an x component of the flow velocity v_x. So, the accelerated flow is a part of the rotational flow around the vortex center. Figure 11(c) shows the same profiles at $x=-10a$ and at $T=230$. The p, ρ, B_z, and T_p have minima at $y\sim 10a$, owing to a fast magnetosonic rarefaction, and they have almost flat broad maxima at $y\sim 45a$. The flow is accelerated strongly at $0<y<20a$ and the peak of the normalized v_y component reaches as large as 1.4. Since the original flow speed at $T=0$ did not exceed 1.0, this is strong evidence that the compressible K–H instability in the transverse configuration leads to a plasma flow acceleration or the flow enhancement near the periphery of the vortex, owing to the fast magnetosonic rarefaction. In other words, where the perturbed vortex motion associated with the excited fast wave is in the same direction as the background flow, the flow velocity is enhanced or the plasma is accelerated.

Figure 12(a) shows temporal evolution of the Reynolds (tangential) stress (momentum flux) $\tau=\langle \rho v_x v_y \rangle$ at $x=0$,

where the angular brackets denote the spatial average over the y direction. The Reynolds stress is normalized by $\rho_0 V_0^2$. In the present 2-D transverse configuration, we obtain from (2),

$$\frac{\partial}{\partial t}\langle \rho v_y \rangle = -\frac{\partial}{\partial x}\langle \rho v_x v_y \rangle. \tag{34}$$

Therefore, the Reynolds stress is responsible for the momentum transport.[13,17,21,101,102] During the initial linear phase the Reynolds stress grows exponentially and after reaching a peak it decreases toward zero. The Reynolds stress becomes zero at $T\sim 30$, when the amplitude of the fundamental mode reaches its peak (see Fig. 4). When the vortices begin to coalesce or when the amplitude of the first subharmonic exceeds the amplitude of the fundamental mode (see Fig. 4), the Reynolds stress begins to increase again at $T\sim 40$. After reaching a peak amplitude at $T\sim 50$ the Reynolds stress decreases and becomes zero at $T\sim 55$, when the amplitude of the first subharmonic reaches its peak. Thereafter, the Reynolds stress oscillates back and forth across zero. The Reynolds stress begins to increase when the amplitude of the second subharmonic exceeds that of the first subharmonic at $T\sim 120$ (see Fig. 4). After reaching a peak at $T\sim 140$ the Reynolds stress becomes zero at $T\sim 150$, when the second subharmonic amplitude reaches its peak (see Fig. 4). Figure 12(b) shows the time integral of the averaged Reynolds stress τ at $x=0$, which is equal to the increase of the total flow momentum in the positive y direction in $x>0$ and is normalized by $20aL_y\rho_0 V_0$. As long as the perturbation is growing or the vortex pairing continues, the total flow momentum in the y direction in $x>0$ increases. Therefore, the net momentum transport from $x<0$ to $x>0$ occurs by the instability. But after the completion of the second vortex pairing at $T\sim 230$, the Reynolds stress becomes very small and the total flow momentum in $x>0$ stays nearly at a constant value. This means that after the completion of the second vortex pairing the net momentum transport vanishes, because no more vortex pairing or no more growth of a subharmonic with $k=k_{\mathrm{FGM}}/8$ is allowed in the system, owing to the finite L_y. Notice that the total flow momentum in the positive y direction in $x>0$ has peaks at $T\sim 30$, 60, and 150, when the amplitudes of the fundamental mode, the first subharmonic, and the second subharmonic have their peak values, respectively (see Fig. 4), and when the Reynolds stress becomes zero [see Fig. 12(a)].

In order to measure quantitatively the momentum transport by the K–H instability, an anomalous viscosity is defined by the following equation:

$$\nu_{\mathrm{ano}} = -\langle \rho v_x v_y \rangle \left(\frac{d}{dx}\langle \rho v_y \rangle \right)^{-1}. \tag{35}$$

This expression for the anomalous viscosity[17,21] is analogous to the definition of the eddy viscosity[104] in the hydrodynamics. But the eddy viscosity is a semi-empirical constant relating the Reynolds stress to the gradient of the flow momentum linearly, and it is assumed to be constant both in time and in space. Here, the anomalous viscosity (35), which is so called because the vortices excited by the instability rather than the ion–ion Coulomb collision are responsible for the momentum transport, is actually measured from the simulation results, and it depends both on time and on space. Figure 13 shows the temporal evolution of the anomalous viscosity ν_{ano} at $x=0$ defined by (35). The anomalous viscosity is normalized by $2aV_0$. At $T\sim 20$, just before the linearly fastest growing (fundamental) mode saturates, ν_{ano} reaches about $0.03\cdot 2aV_0$. But at $T\sim 50$, when the first vortex pairing begins and the first subharmonic is growing (see Fig. 4), it becomes much larger than that at $T\sim 20$ and reaches about $0.5\cdot 2aV_0$. At $T\sim 140$, when the second vortex pairing begins and when the second subharmonic is still growing, it reaches $\sim 2aV_0$, which is twice as large as the anomalous viscosity at the beginning of the first vortex pairing. Since the anomalous viscosity is defined by (35) and the Reynolds stress $\langle \rho v_x v_y \rangle$ at $x=0$ becomes negative during the course of the evolution of the instability, as shown in Fig. 12(a), the anomalous viscosity becomes negative when the Reynolds stress is negative. During this time the steepening of $\langle v_y \rangle$ rather than the relaxation of $\langle v_y \rangle$ occurs. After the completion of the second vortex pairing by $T\sim 250$, the anomalous viscosity fluctuates around zero with a small amplitude and there is no net momentum transport after $T\sim 250$. It is obvious from this figure that at $T\sim 140$, the anomalous viscosity is about twice as large as that at $T\sim 50$. Since Fig. 12(a) shows that the peaks of the Reynolds stress at $x=0$ at $T\sim 50$ and $T\sim 140$ are comparable, the difference of the peak values of the anomalous viscosity at $T\sim 50$ and $T\sim 140$ is due to the difference of the gradient of the flow momentum or $d/dx\langle \rho v_y \rangle$ at $x=0$ in (35). That is, the mean shear of the flow velocity at $T\sim 50$ is twice as large as that at $T\sim 140$. Therefore, the mean shear of the flow velocity is reduced with time or the shear of the flow velocity is relaxed with time.

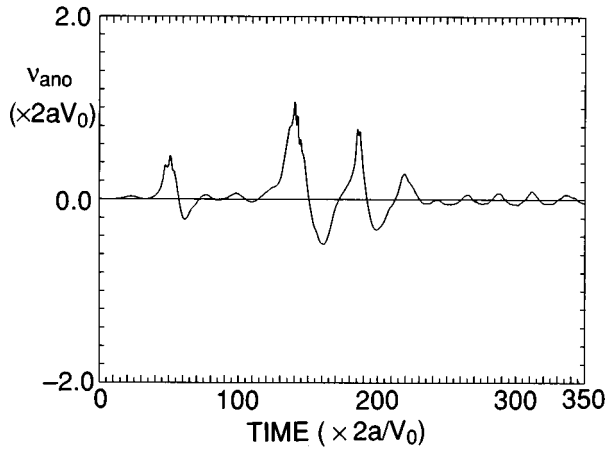

FIG. 13. Temporal evolution of the normalized anomalous viscosity at $x=0$ as a function of the normalized time.

Figure 14 shows, from the top, profiles at $T=20$ [Fig. 14(a)] and $T=220$ [Fig. 14(b)] across x of the Reynolds stress normalized by $\rho_0 V_0^2$, the x component of the electric field $\langle E_x \rangle$ normalized by $V_0 B_0$, which is responsible for the $\mathbf{E}\times\mathbf{B}$ drift in the y direction, the flow momentum profile $\langle \rho v_y \rangle$ normalized by $\rho_0 V_0$, and the flow velocity profile $\langle v_y \rangle$ normalized by V_0. The dotted profiles in $\langle \rho v_y \rangle$ and

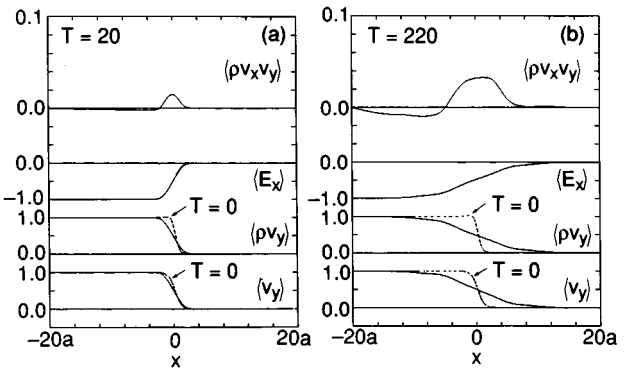

FIG. 14. Profiles at (a) $T=20$ and (b) $T=220$ across x of the averaged Reynolds stress $\langle \rho v_x v_y \rangle$, the x component of the averaged electric field $\langle E_x \rangle$, the averaged flow momentum $\langle \rho v_y \rangle$, and the averaged flow velocity $\langle v_y \rangle$ from the top. The dotted profiles show their initial ($T=0$) profiles.

$\langle v_y \rangle$ show their initial profiles. Although the net momentum is transported from $x<0$ to $x>0$ by the growth of the fastest growing mode at $T=20$ [Fig. 14(a)],[17,21] much larger flow momentum is transported across $x=0$ by the coalescence of the fastest growing modes or by the growth of the second subharmoic at $T=220$ [Fig. 14(b)]. Therefore, a much larger relaxation of the gradient of the average of the flow momentum $\langle \rho v_y \rangle$ and $\langle v_y \rangle$ occurs at $T=220$ [Fig. 14(b)]. Notice that at $T=220$ [Fig. 14(b)] there is a large penetration of $\langle E_x \rangle$ into the region of $x>0$, which is responsible for the momentum transport from $x<0$ to $x>0$.

VI. DISCUSSION AND SUMMARY

Throughout the simulation run presented in Sec. V, the ratio of specific heats Γ was fixed to $\frac{5}{3}$. In order to investigate the dependence of the simulation results on Γ, simulation runs for $\Gamma=\frac{4}{3}$ and $\frac{6}{3}$ $(=2)$ were performed. Those simulation runs for different Γ have shown that the temporal evolution of the instability, including vortex pairing, and the properties of the anomalous momentum transport such as the evolution of the Reynolds stress and the anomalous viscosity, are insensitive to the change of Γ from $\frac{4}{3}$ to 2. Only a slightly noticeable change is that the spatial variation of the temperature due to the development of the instability is smaller for smaller Γ. This is easily expected, because $\Gamma=1$ corresponds to the isothermal equation of state. Therefore the main results presented in the present paper are rather insensitive to the equation of state. Furthermore, in order to see the effect of changing the boundary position in the x direction, a simulation run was performed for $x_b=40a$, that is, by doubling the length of the simulation box in the x direction. The temporal evolution of $|v_x|_{\max}$, the vorticity contours, and the Reynolds stress at $x=0$ was found to be almost the same as the case with $x_b=20a$ presented in the present paper. Therefore, the boundary position in the present simulation run for $x_b=20a$ is considered to be far enough from the velocity shear region to allow the unrestricted growth of the vortex.

The present simulation shows that the vortex pairing indeed occurs in the nonlinear stage of the K–H instability when the convective fast magnetosonic Mach number is up to 0.35. To know whether the vortex pairing occurs or not in the K–H instability in the 2-D transverse configuration for a much higher convective Mach number requires simulation runs for higher convective Mach numbers. It should be noted, however, that hydrodynamic experiments of the spatial evolution of the K–H instability[64,70] show that, although for a small Mach number, coherent, ordered large-scale vortex-like structures appear in the flow, these structures become less noticeable in a high sonic Mach number flow. Those experiments also show that for a high sonic Mach number flow, the widening of the turbulent region with the distance in the spatial evolution of the K–H instability is much smaller than that in the small Mach number flow. These experimental results seem to be consistent with the analysis in Sec. III, which shows that the enstrophy is not an invariant in the 2-D compressible fluid.

Figures 10 and 11 show that the plasma flow velocity v_y is enhanced (the bulk velocity of the plasma is accelerated) at the periphery of the flow vortex. At $T=20$, when four vortices appeared, the flow enhancement is small (see Fig. 10). But at $T=230$ (see Fig. 11), after four vortices coalesced to form a single isolated large vortex, the flow enhancement (in v_y) in the fast rarefaction region inside the vortex becomes as large as $\sim$40% and the flow velocity v_y is reduced considerably in the fast magnetosonic compression region between the vortices [Fig. 11(c)]. These observations suggest that the flow enhancement at the periphery of the flow vortex inside the fast rarefaction region becomes larger with the coalescence of vortices. They also suggest that the decrease of the pressure, density, B_z, and temperature in the fast rarefaction region inside the vortices becomes larger with the coalescence of vortices. Such strong plasma acceleration or the flow enhancement at the periphery of the vortex by the K–H instability, which was first noted by MHD simulation,[17,21] has also been found in a hybrid simulation.[32] In their hybrid simulation for the 2-D transverse configuration, the accelerated flow speed becomes almost twice as large as the original flow velocity when more than eight vortices were accommodated initially in the simulation box. Although their simulation did not clarify the reduction of the density, magnetic field strength, temperature, and the pressure inside the flow vortex due to the fast magnetosonic rarefaction, the appearance of a strong enhancement of the flow velocity in their simulation occurs at the periphery of the vortex and is possibly due to the fast rarefaction process, which is clarified in the present study. Since the sound speed and the Alfvén speed decrease and the plasma flow velocity increases in the fast rarefaction region with the development of the K–H instability, the flow velocity eventually becomes larger than the fast magnetosonic mode speed in the fast rarefaction region and a fast shock discontinuity will be formed in the fast rarefaction region. Such a formation of the fast shock discontinuity in the fast rarefaction region formed by the K–H instability was demonstrated for the flow with larger Mach numbers $M_S=M_A=2.0$ or $M_f=1.41$ $(M_{fc}=0.705)$.[17,21] We expect that such a fast shock is formed for smaller Mach numbers when the vortex pairing is allowed and hence the flow enhancement and the fast rarefaction inside the vortex become much stronger than the case without the vortex pairing.

Although a notion that the magnitude of the turbulent viscosity due to turbulent eddies is of the order of $\Delta L \cdot \Delta V$, where ΔL is the characteristic scale length of the flow and ΔV is the variation of the mean velocity over the distance ΔL, which is nearly equal to the size of the largest eddy in the turbulence, is not new,[2] the present simulation measures quantitatively the magnitude of the anomalous viscosity ν_{ano} by the K–H instability and its increase with the vortex pairing and the growth of the subharmonic modes (see Fig. 13). Figure 13 shows that when the linearly fastest growing mode (vortex) is growing the anomalous viscosity ν_{ano} at $x=0$ reaches $\sim 0.03 \cdot 2aV_0$. But when the first vortex pairing begins it reaches $\sim 0.5 \cdot 2aV_0$, owing to the growth of the first subharmonic, and when the second vortex pairing begins it reaches $\sim 2aV_0$, owing to the growth of the second subharmonic. If a further vortex pairing and a growth of a subharmonic with a longer wavelength is allowed, the anomalous viscosity will become larger than $\sim 2aV_0$. Therefore, the momentum transport and the anomalous viscosity by the K–H instability become larger and larger with the vortex pairing and the growth of subharmonics, and the velocity shear layer becomes wider and wider with the vortex pairing and the growth of subharmonics. Such tendency of the widening of the velocity shear layer with the vortex pairing and the growth of subharmonics is apparent in a hydrodynamic experiment of the shear instability,[64] although their experiment showing a spatial development of the K–H instability did not show explicitly a widening of the velocity shear layer. For a different MHD configuration, wherein the magnetc field is parallel to the flow, the widening of the velocity shear layer by the K–H instability with the vortex pairing has been demonstrated by MHD simulations,[23,26] although their simulations did not measure quantitatively the anomalous viscosity. The anomalous momentum transport by the K–H instability evaluated in the present simulation up to when the fundamental mode saturates is essentially a quasilinear momentum transport due to the fastest growing vortices, which are inclined with respect to the zeroth-order flow. This has been formulated previously.[13,101–103] Even after the inverse energy cascade or the vortex pairing in the 2-D K–H instability, a larger momentum transport and a larger anomalous viscosity than the quasilinear transport seems to be due to the coherent inclination of the largest vortex in the flow and the growth of the corresponding subharmonic. Therefore, a coherent transport of the flow momentum demonstrated in the present simulations may be the real nature of the anomalous momentum transport in the 2-D shear flow. It should be noted in the present simulation run that the vortex pairing begins with the substantial growth of the corresponding subharmonic. Therefore, although the vortex pairing involves essentially nonlinear interactions, it is closely related to the growth of subharmonic modes, as has been discussed by Ho.[67] That is, the subharmonic can be viewed as a catalyst of the vortex pairing. In his conceptual subharmonic evolution model (see Fig. 30 of Ho and Huang[67]), however, he assumed that the final amplitudes of all subharmonics were equal and also that the vortex pairing occurred when the corresponding subharmonic reached a peak amplitude. However, according to the present simulation results the final amplitudes of subharmonics reached in the development of the instability are larger for a longer wavelength (see Fig. 4), and this is responsible for the increase of the anomalous viscosity with the vortex pairing. Also, the present simulation clearly shows that the vortex pairing begins and ends in a finite time interval.

In practical problems the spatial growth of the K–H instability[23,31,32,64,70] is more common than the temporal growth as treated here. In such spatial growth of the K–H instability, the large momentum transport by the K–H instability and the vortex pairing is expected in the downstream region of the sheared plasma flow. Let us transform the present results of the widening of the velocity shear layer obtained in the temporal growth of the K–H instability into a spatial growth. Figure 14 shows that at $T=220$ the thickness of the velocity shear layer D_{VSL} is $\sim 24a$. Since the phase velocity of the K–H vortex is $V_0/2$, the distance D_y over which the wave or the vortex traverses during the time interval of $220 \times 2a/V_0$ is $D_y=(220\times 2a/V_0)\times V_0/2=220a$. Therefore, in the spatial development of the K–H instability the ratio D_{VSL}/D_y would be nearly equal to $24a/220a=0.109$. Notice that this ratio in the scaling law is irrespective of the initial thickness of the velocity shear layer. This is because when the initial thickness of the velocity shear layer is smaller, the growth rate of the K–H instability is larger (see Sec. IV), and the widening of the velocity shear layer occurs more rapidly. Therefore, D_{VSL}/D_y does not depend on the initial thickness of the velocity shear layer. But in order to get a more accurate value of D_{VSL}/D_y a much larger simulation run, which may accommodate, for example, eight vortices in the linear stage, is necessary.

In summary, for the 2-D MHD transverse configuration in a compressible plasma or in a 2-D fluid, the conservation law of the enstrophy is derived and 2-D MHD simulations have been performed. The present study shows that when the plasma (fluid) is compressible or when the baroclinic vector is nonzero, the enstrophy is not an invariant of the 2-D plasma (fluid) motion. The 2-D MHD simulations have been performed for the fast magnetosonic convective Mach number 0.35. The simulation results show that after the linear growth and the subsequent nonlinear saturation of the fastest growing (fundamental) mode (vortex) the vortex train formed by the K–H instability is further susceptible to the vortex pairing, which continues as long as the length of the simulation system allows it, and the vortex pairing occurs due to the growth of subharmonics. In the 2-D transverse configuration the eddy current, which is inertia current in nature, is associated with each flow vortex and the current eddies also coalesce to form a large isolated current eddy. Inside the vortex or the current eddy the plasma is rarefied by the fast magnetosonic rarefaction. That is, the centrifugal force due to the vortex rotation is balanced with the sum of the $\mathbf{J}\times\mathbf{B}$ force and the $-\nabla p$ force. In the fast rarefaction region the pressure, density, magnetic field strength, and temperature decrease and the plasma flow velocity inside the fast rarefaction region near the periphery of the vortex increases due to a superposition of the perturbed vortex motion associated with the fast magnetosonic (rarefaction) wave to the zeroth-order flow. The rarefaction of the plasma and the

flow enhancement inside the vortex become stronger and stronger with the development of the vortex pairing. The net transport of momentum across the initial velocity shear layer occurs when the fundamental mode or the subharmonic is growing and when the vortex pairing continues. The momentum transport resulting in a velocity shear relaxation by the vortex pairing is much larger than that due to the growth of the fundamental mode. The anomalous viscosity by the K–H instability is defined using the Reynolds stress and is measured quantitatively from the simulation result. The anomalous viscosity becomes larger and larger with the vortex pairing and this is due to the growth of subharmonics. After two consecutive vortex pairings the anomalous viscosity reaches as large as $2aV_0$, where $2a$ is the initial thickness of the velocity shear layer and V_0 is the total jump of the flow velocity across the velocity shear layer. It is found that the simulation results are rather insensitive to the choice of the ratio of specific heats Γ (at least from $\frac{4}{3}$ to 2). In order to check whether or not the vortex pairing (vortex condensation in real space) is inhibited for a higher Mach number shear flow, more simulation runs for higher Mach numbers are necessary.

ACKNOWLEDGMENTS

The author wishes to thank the referee for his/her illuminating comments, which have helped improve the manuscript greatly. The computation for this work was performed at the computer center of the University of Tokyo.

This work has been supported by Grants-in-Aid for Scientific Research No. 06640566 and No. 09640529, provided by the Ministry of Education, Science, Sports, and Culture, and, in part, by the Radio Atmospheric Center of Kyoto University and the Institute of Space and Astronautical Science of the Ministry of Education, Science, Sports, and Culture as a joint research project.

[1] S. Chandrasekhar, *Hydrodynamic and Hydromagnetic Stability* (Oxford University Press, Oxford, 1961), Chap XI.
[2] L. D. Landau and E. M. Lifshitz, *Fluid Mechanics* (Pergamon, Oxford, 1959).
[3] R. A. Gervin, Rev. Mod. Phys. **40**, 652 (1968).
[4] A. Hasegawa, *Plasma Instabilities and Nonlinear Effects* (Springer-Verlag, Berlin, 1975), p. 125.
[5] D. J. Tritton, *Physical Fluid Dynamics* (Van Nostrand Reinhold, Berkshire, England, 1977), p. 209.
[6] J. W. Dungey, in *Proceedings of the Conference of the Ionosphere* (The Physical Society, London, 1955), p. 225.
[7] J. A. Fejer, Phys. Fluids **7**, 499 (1964).
[8] S. P. Talwar, J. Geophys. Res. **69**, 2707 (1964).
[9] A. K. Sen, Planet. Space Sci. **13**, 131 (1965).
[10] I. Lerche, J. Geophys. Res. **71**, 2365 (1966).
[11] D. J. Southwood, Planet. Space Sci. **16**, 587 (1968).
[12] M. Dobrowolny, Phys. Fluids **15**, 2263 (1972).
[13] A. Miura and T. Sato, J. Geophys. Res. **83**, 2109 (1978).
[14] T. Tajima and J. N. Lebouef, Phys. Fluids **23**, 884 (1980).
[15] A. D. M. Walker, Planet. Space Sci. **29**, 1119 (1981).
[16] J. D. Huba, J. Geophys. Res. **86**, 8991 (1981).
[17] A. Miura, Phys. Rev. Lett. **49**, 779 (1982).
[18] A. Miura and P. L. Pritchett, J. Geophys. Res. **87**, 7431 (1982).
[19] J. S. Wagner, R. D. Sydora, T. Tajima, T. Hallinan, L. C. Lee, and S.-I. Akasofu, J. Geophys. Res. **88**, 8013 (1983).
[20] Z. Y. Pu and M. G. Kivelson, J. Geophys. Res. **88**, 841 (1983).
[21] A. Miura, J. Geophys. Res. **89**, 801 (1984).
[22] P. L. Pritchett and F. V. Coroniti, J. Geophys. Res. **89**, 168 (1984).
[23] C. C. Wu, J. Geophys. Res. **91**, 3042 (1986).
[24] A. Miura, J. Geophys. Res. **92**, 3195 (1987).
[25] G. Y. Ganguli, , Y. C. Lee, and P. J. Palmadesso, Phys. Fluids **31**, 823 (1988).
[26] G. Belmont and G. Chanteur, Phys. Scr. **40**, 124 (1989).
[27] V. A. Thomas and D. Winske, Geophys. Res. Lett. **18**, 1943 (1991).
[28] A. Miura, J. Geophys. Res. **97**, 10 655 (1992).
[29] T. Terasawa, M. Fujimoto, H. Karimabadi, and N. Omidi, Phys. Rev. Lett. **68**, 2778 (1992).
[30] Z. Wang, P. L. Pritchett, and M. Ashour-Abdalla, Phys. Fluids B **4**, 1092 (1992).
[31] J. R. Manuel and J. C. Samson, J. Geophys. Res. **98**, 17 367 (1993).
[32] V. A. Thomas and D. Winske, J. Geophys. Res. **98**, 11 425 (1993).
[33] M. Fujimoto and T. Terasawa, J. Geophys. Res. **99**, 8601 (1994).
[34] M. Wilber and R. M. Winglee, J. Geophys. Res. **100**, 1883 (1995).
[35] A. Miura, in *Physics of the Magnetopause*, edited by P. Song, B. U. Ö. Sonnerup, and M. F. Thomsen (American Geophysical Union, Washington, DC, 1995), p. 285.
[36] J. D. Huba, Geophys. Res. Lett. **21**, 2907 (1996).
[37] P. H. Yoon, J. F. Drake, and A. T. Y. Lui, J. Geophys. Res. **101**, 27 327 (1996).
[38] K. W. Min and D. Y. Lee, Geophys. Res. Lett. **23**, 3667 (1996).
[39] M. J. Keskinen, Phys. Plasmas **3**, 1259 (1996).
[40] E. T. Scharlemann, Astrophys. J. **219**, 617 (1978).
[41] P. Ghosh and F. K. Lamb, Astrophys. J. **232**, 259 (1979).
[42] U. Anzer and G. Börner, Astron. Astrophys. **83**, 133 (1980).
[43] Y.-M. Wang and J. A. Robertson, Astron. Astrophys. **139**, 93 (1984).
[44] S. R. Choudhury and R. V. E. Lovelace, Astrophys. J. **302**, 188 (1986).
[45] J. Arons, Astrophys. J. **408**, 160 (1993).
[46] J. T. Karpen, S. K. Antiochos, R. B. Dahlburg, and D. S. Spicer, Astrophys. J. **403**, 769 (1993).
[47] D. Ryu, T. W. Jones, and A. Frank, Astrophys. J. **452**, 785 (1995).
[48] A. Malagoli, G. Bodo, and R. Rosner, Astrophys. J. **456**, 708 (1996).
[49] A. Frank, T. W. Jones, D. Ryu, and J. B. Gaalaas, Astrophys. J. **460**, 777 (1996).
[50] T. W. Jones, J. B. Gaalaas, D. Ryu, and A. Frank, Astrophys. J. **482**, 230 (1997).
[51] N. D'Angelo, Phys. Fluids **8**, 1748 (1965).
[52] C. G. Smith and S. von Goeler, Phys. Fluids **11**, 2665 (1968).
[53] J. A. Byers, Phys. Fluids **9**, 1038 (1966).
[54] R. H. Levy and R. W. Hockney, Phys. Fluids **11**, 766 (1968).
[55] F. W. Perkins and D. L. Jassby, Phys. Fluids **14**, 102 (1971).
[56] K. Theilhaber and C. K. Birdsall, Phys. Fluids B **1**, 2260 (1989).
[57] T. Tajima, W. Horton, P. J. Morrison, J. Schutkeker, T. Kamimura, K. Mima, and Y. Abe, Phys. Fluids B **3**, 938 (1991).
[58] H. Romero, G. Ganguli, and Y. C. Lee, Phys. Rev. Lett. **69**, 3503 (1992).
[59] D. Cai, L. R. O. Storey, and T. Itoh, Phys. Fluids B **5**, 3507 (1993).
[60] V. Gavrishchaka, M. E. Koepke, J. J. Carroll, III, and G. Ganguli, in *Cross-Scale Coupling Processes in Space Plasma*, edited by J. Horwitz, N. Singh, and J. Burch (American Geophysical Union, Washington, DC, 1995), p. 81.
[61] N. J. Zabusky and G. S. Deem, J. Fluid Mech. **47**, 353 (1971).
[62] J. P. Christiansen and N. J. Zabusky, J. Fluid Mech. **61**, 219 (1973).
[63] C. D. Winant and F. K. Browand, J. Fluid Mech. **63**, 237 (1974).
[64] G. L. Brown and A. Roshko, J. Fluid Mech. **64**, 775 (1974).
[65] F. K. Browand and P. D. Weidman, J. Fluid Mech. **76**, 127 (1976).
[66] P. G. Drazin and A. Davey, J. Fluid Mech. **82**, 255 (1976).
[67] C.-M. Ho and L.-S. Huang, J. Fluid Mech. **119**, 443 (1982).
[68] G. M. Corcos and F. S. Sherman, J. Fluid Mech. **139**, 29 (1984).
[69] H. T. Moon and P. D. Weidman, Phys. Fluids **31**, 3804 (1988).
[70] D. Papamoshou and A. Roshko, J. Fluid Mech. **197**, 453 (1988).
[71] S. Lele, *27th Aerospace Science Meeting* (American Institute of Aeronautics and Astronautics, Inc., Washington DC, 1989), Paper No. 89-0374.
[72] N. D. Sandam and W. C. Reynolds, AIAA J. **28**, 618 (1990).
[73] N. D. Sandam and W. C. Reynolds, J. Fluid Mech. **224**, 133 (1991).
[74] W. I. Axford and C. O. Hines, Can. J. Phys. **39**, 1433 (1961).
[75] P. H. Reiff, R. W. Spiro, and T. W. Hill, J. Geophys. Res. **86**, 7639 (1981).
[76] R. P. Lepping and L. F. Burlaga, J. Geophys. Res. **84**, 7099 (1979).
[77] S.-H. Chen, M. G. Kivelson, J. T. Gosling, R. J. Walker, and A. J. Lazarus, J. Geophys. Res. **98**, 5727 (1993).
[78] S.-H. Chen and M. G. Kivelson, Geophys. Res. Lett. **20**, 2699 (1993).
[79] S. Kokubun, H. Kawano, M. Nakamura, T. Yamamoto, K. Tsuruda, H.

Hayakawa, A. Matsuoka, and L. A. Frank, Geophys. Res. Lett. **21**, 2883 (1994).
[80]H. Kawano, S. Kokubun, T. Yamamoto, K. Tsuruda, H. Hayakawa, M. Nakamura, T. Okada, A. Matsuoka, and A. Nishida, Geophys. Res. Lett. **21**, 2895 (1994).
[81]F. S. Mozer, K. Tsuruda, H. Hayakawa, M. Nakamura, S. Kokubun, and T. Yamamoto, Geophys. Res. Lett. **21**, 2983 (1994).
[82]J. Seon, L. A. Frank, J. T. Gosling, A. J. Lazarus, R. P. Lepping, and C. T. Russell, J. Geophys. Res. **100**, 11 907 (1995).
[83]M. G. Kivelson and S.-H. Chen, in Ref. 35, p. 257.
[84]A. W. Schardt, K. W. Behannon, R. P. Lepping, J. F. Carbary, A. Eviatar, and G. L. Siscoe, in *Saturn*, edited by T. Gehrels and M. S. Matthews (University of Arizona Press, Tucson, 1984), p. 416.
[85]D. A. Roberts, M. L. Goldstein, W. H. Matthaeus, and S. Ghosh, J. Geophys. Res. **97**, 17 115 (1992).
[86]M. L. Goldstein, D. A. Roberts, and W. H. Matthaeus, Annu. Rev. Astron. Astrophys. **33**, 283 (1995).
[87]K. H. Burrell E. J. Doyle, P. Gohill, R. J. Groebner, J. Kim, R. J. LaHaye, L. L. Lao, R. A. Moyer, T. H. Osborne, W. A. Peebles, C. L. Rettig, T. H. Rhodes, and D. M. Thomas, Phys. Plasmas **1**, 1536 (1994).
[88]J. R. Spreiter, A. L. Summers, and A. Y. Alksne, Planet. Space Sci. **14**, 14223 (1966).
[89]L. Onsager, Nuovo Cimento Suppl. **6**, 279 (1949).
[90]G. K. Batchelor, *The Theory of Homogeneous Turbulence* (Cambridge University Press, Cambridge, 1953), p. 187.
[91]R. H. Kraichnan, Phys. Fluids **10**, 1417 (1967).
[92]D. C. Montgomery, in *Nagoya Lectures in Plasma Physics and Controlled Fusion*, edited by Y. H. Ichikawa and T. Kamimura (Tokai University Press, Tokai, 1989), p. 207.
[93]D. Biskamp, *Nonlinear Magnetohydrodynamics* (Cambridge University Press, Cambridge, 1993), Chap. 7.
[94]G. Vahala and D. Montgomery, J. Plasma Phys. **6**, 425 (1971).
[95]T. E. Eastman, Phys. Fluids B **5**, 2671 (1993).
[96]A. Eviatar and R. W. Wolf, J. Geophys. Res. **73**, 5561 (1968).
[97]B. T. Tsurutani and R. M. Thorne, Geophys. Res. Lett. **9**, 1247 (1982).
[98]R. A. Treumann, J. Labelle, and R. Pottelette, J. Geophys. Res. **96**, 16 009 (1991).
[99]H. Okuda, J. Geophys. Res. **98**, 3953 (1993).
[100]D. Winske, V. A. Thomas, and N. Omidi, in Ref. 35, p. 321.
[101]A. Miura and T. Sato, J. Fluid Mech. **86**, 33 (1978).
[102]W. Horton, T. Tajima, and T. Kamimura, Phys. Fluids **30**, 3485 (1987).
[103]R. Rankin, P. Frycz, J. C. Samson, and V. T. Tikhonchuk, Phys. Plasmas **4**, 829 (1997).
[104]H. Lamb, *Hydrodynamics*, 6th ed. (Cambridge University Press, London, 1932), p. 668.
[105]S. I. Braginskii, in *Reviews of Plasma Physics*, edited by M. A. Leontovich (Consultants Bureau, New York, 1965), Vol. 1, p. 205.
[106]A. Michalke, J. Fluid Mech. **19**, 543 (1964).